Upper Mantle Discontinuity Topography from Thermal and Chemical Heterogeneity

Nicholas Schmerr, *et al.*

Science **318**, 623 (2007);
DOI: 10.1126/science.1145962

Science (print ISSN 0036-8075; online ISSN 1095-9203) is published weekly, except the last week in December, by the American Association for the Advancement of Science, 1200 New York Avenue NW, Washington, DC 20005.

Upper Mantle Discontinuity Topography from Thermal and Chemical Heterogeneity

Nicholas Schmerr* and Edward J. Garnero

Using high-resolution stacks of precursors to the seismic phase *SS*, we investigated seismic discontinuities associated with mineralogical phase changes approximately 410 and 660 kilometers (km) deep within Earth beneath South America and the surrounding oceans. Detailed maps of phase boundary topography revealed deep 410- and 660-km discontinuities in the down-dip direction of subduction, inconsistent with purely isochemical olivine phase transformation in response to lowered temperatures. Mechanisms invoking chemical heterogeneity within the mantle transition zone were explored to explain this feature. In some regions, multiple reflections from the discontinuities were detected, consistent with partial melt near 410-km depth and/or additional phase changes near 660-km depth. Thus, the origin of upper mantle heterogeneity has both chemical and thermal contributions and is associated with deeply rooted tectonic processes.

Globally imaged upper mantle seismic discontinuities (*1*) observed at depths near 410, 520, and 660 km arise from mineralogic phase transformations of the mineral olivine to wadsleyite, wadsleyite to ringwoodite, and ringwoodite to perovskite + magnesiowüstite, respectively (*2*) (Fig. 1A). For simplicity, we refer to each discontinuity by an average depth, for example, "410 km" and "660 km," although the exact depth of each boundary varies. The region between 410 km and 660 km is known as the mantle transition zone (MTZ). The slope of the phase transition boundary in pressure-temperature space, that is, the Clapeyron slope, is positive for the olivine-to-wadsleyite transition (*3*), resulting in a shallower 410-km discontinuity in cold regions and a deeper 410 km in hot areas. The ringwoodite-to-perovskite phase transition has a negative Clapeyron slope (*4*); therefore, the 660 km is deeper in cold areas and shallower in hot regions. Consequently, 410- and 660-km depth perturbations are opposite and anticorrelated for thermal anomalies extending across the MTZ, which has been used in past studies to infer mantle temperature [e.g., (*5*–*8*)].

We investigated upper mantle structure beneath South America and the surrounding oceans, a region with prolonged subduction of the Nazca plate along the western coast of South America, mid-ocean spreading centers at the mid-Atlantic ridge and along the East Pacific Rise, and several volcanic hotspots. Seismic investigations of MTZ thickness and discontinuity structure beneath South America have used precursors to the *SS* seismic phase (Fig. 1A), receiver functions (*9*), and near-source reflected and converted waves (*10*, *11*). Past *SS* analyses of this region were global studies (*5*–*7*) reliant on long-period (>25 s) and comparatively sparse data, retrieving long-wavelength structure (typically greater than 2000- to 3000-km lateral scales); receiver function and converted wave analyses provide higher-resolution information but are localized to areas beneath seismographic stations. Where resolved, these studies identified a relatively thick MTZ beneath South American subduction, consistent with the expected presence of a cold slab.

We extended our *SS* precursor method (*12*) to shorter period energy (~10 s) with an order of magnitude more data that past efforts, using broadband data from global earthquake sources (Fig. 1B). Our final data set consists of more than 16,000 high-quality broadband seismograms that densely sample our study region (Fig. 1C). *SS* precursor amplitudes are typically 1 to 10% of the main *SS* amplitude; thus, stacking is necessary to bring precursors out of the background noise (Fig. 1A); we stacked data in 1000-km-radius geographic bins. We exclude epicentral distance windows exhibiting interference between precursors and other seismic phases that can skew predicted discontinuity depths (figs. S1 and S2). Before stacking, corrections for mantle heterogeneity, varying crustal thickness, and surface topography are applied (*13*).

A bootstrap resample (n = 300) (*14*) of seismograms within each bin is used to evaluate whether the 410-km (*S*410*S*) and 660-km (*S*660*S*) precursor stacks amplitudes are above the 95% confidence interval. For each bin, a frequency histogram of bootstrap-predicted precursor depths is constructed from the arrival time of the maximum-stacked amplitude within a ±15 s window around the predicted precursor arrival time in each bootstrap resample. Stacks containing coherent precursory energy display amplitudes well above the 95% confidence interval; at long periods (25 s), calculated discontinuity depth bootstrap histograms display clear single peaks, with the most frequent histogram value nearly identical to the peak precursor energy arrival time from a stack of all data (Fig. 2). However, at shorter periods (10 s), the bootstrap-derived discontinuity depth distributions sometimes reveal a bimodal distribution, implying multiple reflectors. We use such histograms for inferring single versus multiple reflections near the phase boundaries.

Discontinuity depth histograms for bins near specific tectonic features indicate an MTZ generally thickened beneath subduction and slightly thinned beneath mantle hotspots (figs. S3 and S4). The 410-km discontinuity is unexpectedly deep by up to 10 to 15 km just east of the subducting Nazca slab beneath the north and central portion of the South American continent (Fig. 3); this is the opposite of what is expected for a cold MTZ associated with long-lived subduction. The 660-km discontinuity beneath

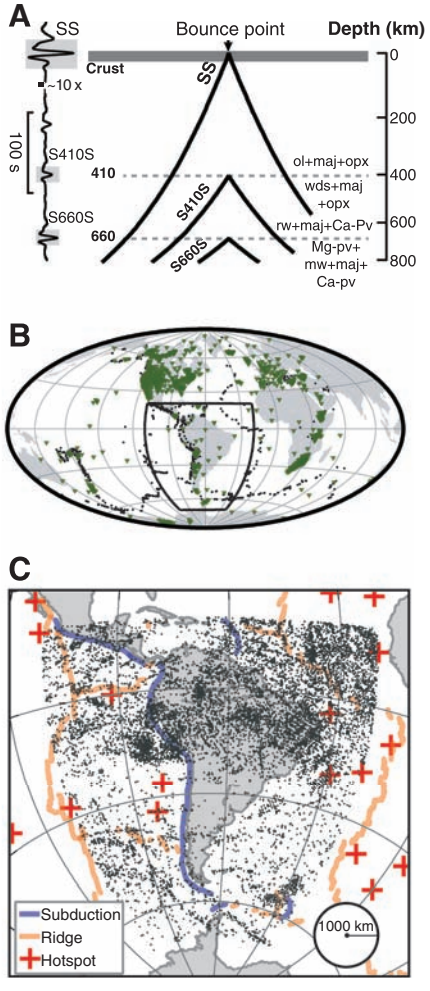

Fig. 1. (**A**) Schematic cross-section of *SS*, *S*410*S*, and *S*660*S* upper mantle ray paths halfway between earthquake and receiver with dominant MTZ mineralogy: olivine (ol), orthopyroxene (opx), majorite (maj), wadsleyite (wds), ringwoodite (rw), Ca-perovskite (Ca-pv), magnesiowüstite (mw), Mg-perovskite (Mg-pv). A synthetic waveform is shown on the left. (**B**) The distribution of earthquakes (black points) and seismic stations (green triangles) used in our study region (outlined box). (**C**) The location of *SS* bounce points (black dots) and major tectonic features (*30*) and hotspots (*31*). A 1000-km-radius bin is shown for scale.

Arizona State University, School of Earth and Space Exploration, Box 871404, Tempe, AZ 85287–1404, USA.

*To whom correspondence should be addressed. E-mail: nschmer@asu.edu

subduction and the South American continent is deepened by 15 to 30 km, consistent with cold material intersecting this boundary. The thickened MTZ (fig. S4) is due to a greater offset of the 660-km discontinuity than for the 410 km. These features are independent of the tomography models used to correct travel times before stacking (fig. S3) and are visible in past studies of this region (*5*, *9*), although those studies focused on MTZ thickness.

In addition to the depressed 410 km to the east of subduction, multiple reflectors on both the 410- and 660-km discontinuities are evident for the 10-s period stacks. This behavior occurs at the intersection of the slab and the 410-km boundary, as indicated by the bimodal distribution in the histogram depths: a shallow reflector at 395- to 400-km depth and a deeper reflector at 410 to 415 km. In several cross-sections, an elevated 410 km from the west overlaps a depressed 410 km to the east. A stepped 410-km discontinuity also appears beneath ridges or hotspots in several cross-sections. Additionally, on the Pacific Ocean side, the 660 km appears as two reflectors, one at 640- to 645-km depth and another at 665- to 670-km depth, up to 3000 km away from the slab. Multiple discontinuities are only apparent with short period data (Fig. 2); these high-resolution shear velocity features have not been previously detected using *SS* precursors. However, some studies of *PP* precursors (*15*), near-source reflected *P* waves (*16*), and receiver function studies (*17*) have noted multiple discontinuities in the vicinity of the major phase boundaries.

The depressed 410-km discontinuity east of a cold subducting Nazca plate cannot be solely explained by a thermal origin. If present, metastable olivine within the slab may depress the 410-km boundary (*18*); however, this effect is confined to within the slab (e.g., 50 to 100 km laterally, not thousands of kilometers). Compositional heterogeneities transported by the sinking slab can perturb phase transition stability, depth, and sharpness (*19*).

Subduction may carry an appreciable amount of H_2O into the MTZ, either within the slab or by viscous entrainment of hydrated mantle wedge material (*20*). Experiments suggest that wadsleyite and ringwoodite are hydrophilic relative to olivine and capable of holding up to several weight percent (wt %) H_2O (*21*, *22*). Increasing H_2O reduces the olivine-to-wadsleyite phase transition depth and deepens that of ringwoodite to perovskite + magnesiowüstite. Thus, elevated hydration thickens the MTZ while reducing MTZ seismic velocity and density (*20*). Hydrated wadsleyite is chemically buoyant compared with its anhydrous counterpart (*22*) and should remain at the top of the MTZ, potentially melting (*23*). Hydrated wadsleyite can seismically mask the 410-km phase boundary if the H_2O concentration is ≥0.75 wt % (fig. S16); the transition from hydrated upper MTZ to less hydrated lower MTZ can produce a seismic impedance contrast consistent with experimental predictions and with our observations. A hydrated "lens" of wadsleyite at the top of the MTZ (Fig. 4 and figs. S16 to S18) can thus appear as a deepened 410-km discontinuity. The large east-west lateral extent of the buoyant hydrated wadsleyite lens is consistent with trench rollback migrating the input of hydrated materials westward. Seismic reflections from the base of the lens should weaken with either decreased H_2O content (as expected to the east away from the slab) or broadening of the wet-to-dry wadsleyite transition. We observe decreased *S*410*S* amplitudes from the large-scale depressed 410-km boundary (fig. S17).

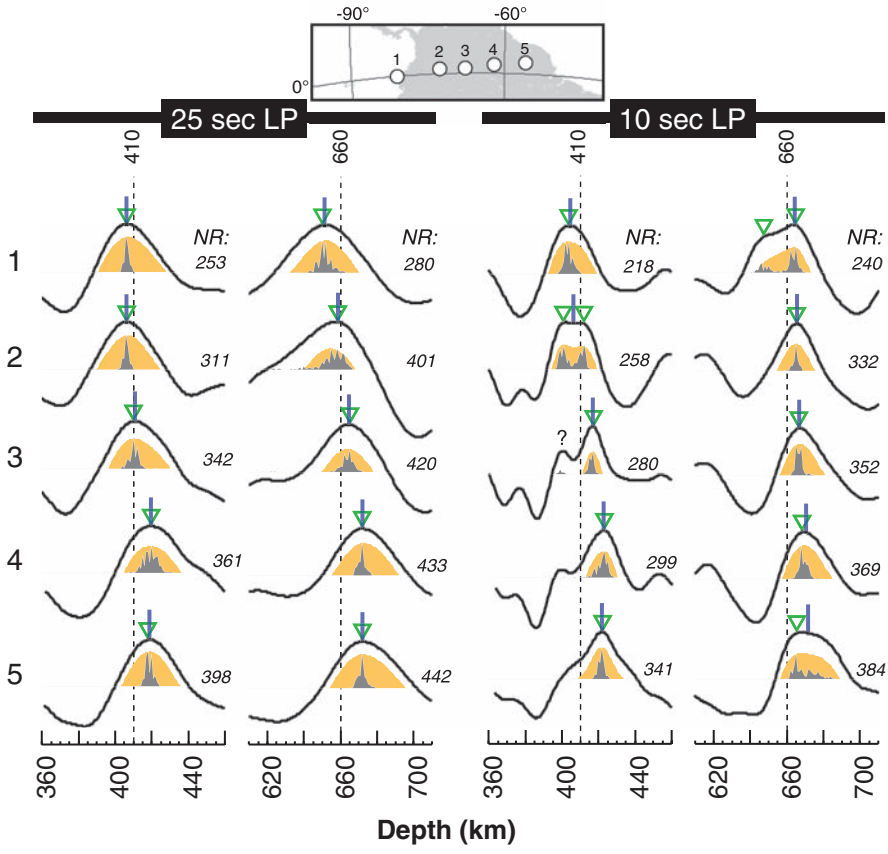

Fig. 2. Histogram stacks for *S*410*S* and *S*660*S* precursors in five example bins (inset map). Data are low-pass filtered at 25 s (left) and 10 s (right). NR is the number of records in each stack. Stacked traces (solid black lines) are underlain by energy falling above the bootstrap 95% confidence interval (orange) and a histogram of the peak bootstrap amplitudes (gray). Discontinuity depths are picked for the peak amplitude of the stacked trace (blue lines) and the mode(s) of the bootstrap resample (green triangles).

Other possibilities can produce topography on the 410-km discontinuity. For example, experimental work on Mg_2SiO_4-Fe_2SiO_4 at high pressures and temperatures finds that enriching Mg relative to Fe increases the pressure of the olivine to wadsleyite phase transition [e.g., (*24*)]. Increasing the Mg content of $(Mg,Fe)_2SiO_4$ from the expected 89% Mg to 92% Mg results in a 7- to 10-km deeper 410-km discontinuity. This is not unexpected, because melting in the overlying mantle wedge preferentially extracts Fe, leaving a magnesium-enriched residue that should be viscously entrained and brought into the MTZ. If trench rollback migrates the input of entrained wedge residue westward, a compositionally varying 410-km discontinuity trough may result (fig. S18D). Both interpretations depend on mantle wedge chemistry, degree of viscous coupling, and the detailed history of trench rollback, which are not precisely known.

The long-wavelength depression on the 660-km discontinuity beneath South America (Fig. 3 and figs. S5 to S15) is consistent with either a remnant thermal anomaly from the previous slab location or past stalling and/or accumulation of slab material at the 660-km discontinuity that has since subducted into the lower mantle. A deepened 410-km discontinuity overlying a wide 660-km discontinuity depression has been similarly observed to the west of Japan (*25*, *26*).

The 660-km discontinuity is elevated 5 to 10 km directly beneath the East Pacific Rise and the Mid-Atlantic Ridge (Fig. 3, profiles A-A′, B-B′, and C-C′). There is evidence for multiple reflections from the 410-km in these regions, consistent with a melt layer in warmer mantle enriched in CO_2 or H_2O (*27*, *28*). It is widely agreed that seismic velocity reductions beneath mid-ocean ridges is confined to the upper few hundred km of the mantle, although a thinned MTZ beneath ridges underlain by an elevated

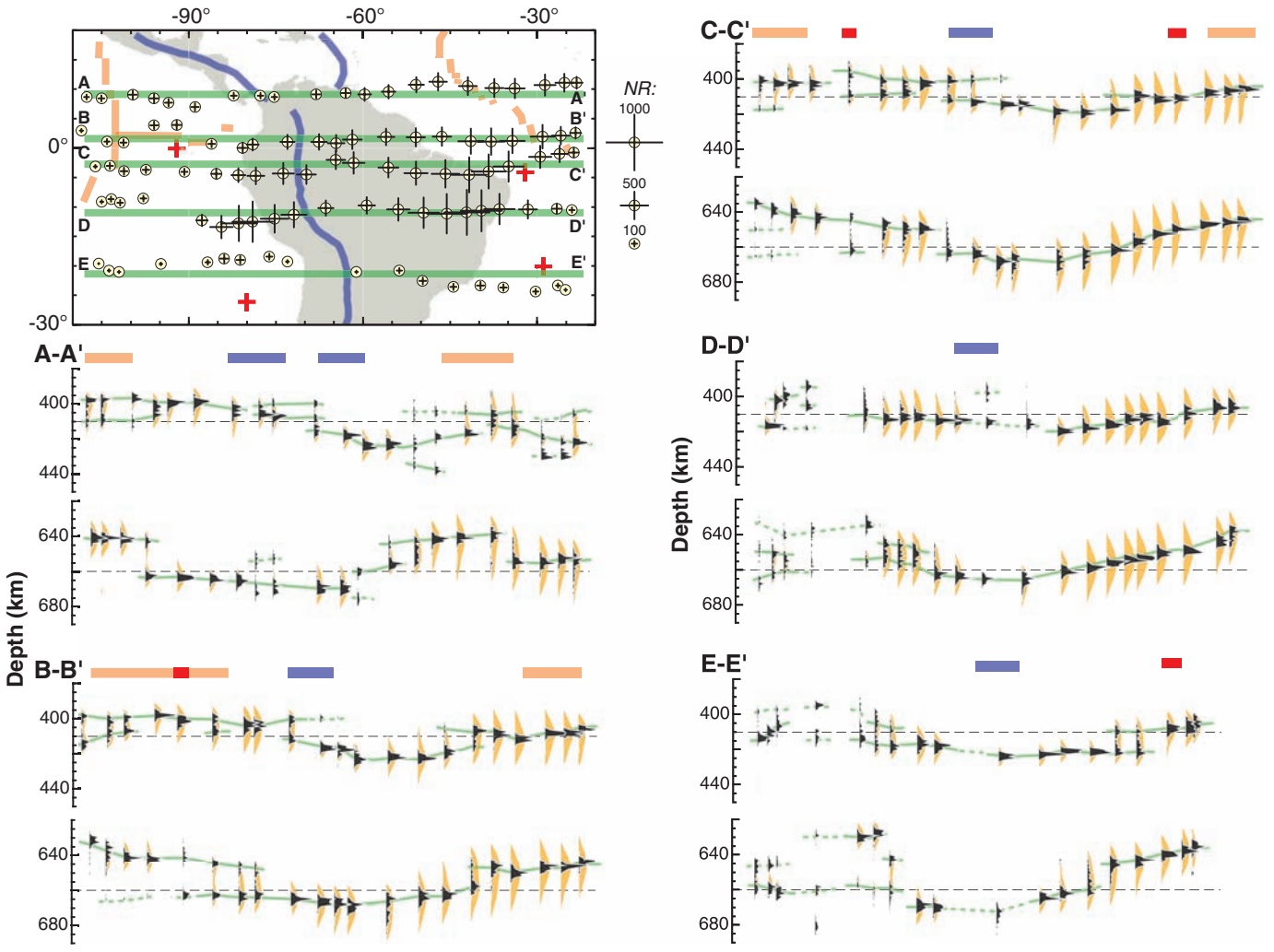

Fig. 3. East-west cross-sections of discontinuity topography and map giving cross-sections (green lines), bin locations (white circles), average record number (black crosses), and surface features (Fig. 1C legend). Discontinuity-depth histograms are plotted (as in Fig. 2) for each bin. Interpreted structure is drawn in green and dotted where less uncertain. Horizontal color bars denote locations of ridges (orange), the estimated location of slabs in the MTZ (blue), and hot spots (red) that intersect cross-sections (see also additional cross-sections in figs. S5 to S15).

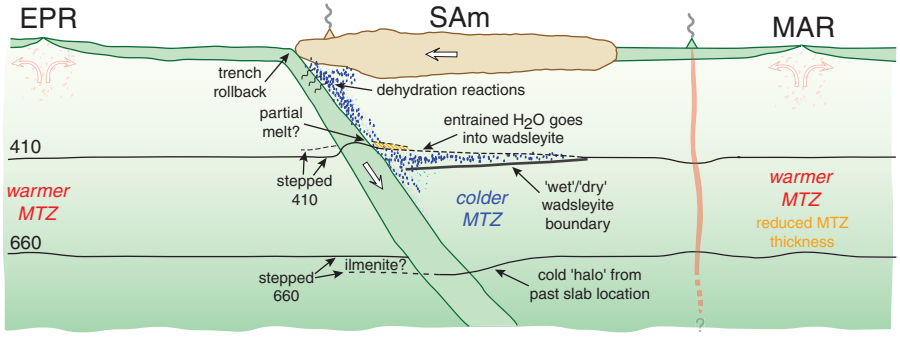

Fig. 4. An H_2O-rich lens underplating the 410-km discontinuity in cross-section view, relative to the East Pacific Rise (EPR), South American continent (SAm) and Mid-Atlantic Ridge (MAR). Trench migration contributes to the hydrated wadsleyite lens evolution, the base of which is detected in our study. The multiplicity of reflectors near 410- and 660-km depths may be explained by partial melt at the 410-km boundary and by the presence of akimotoite below the 660-km discontinuity.

660-km boundary suggests that some MTZ material, at least locally, is warmer than the surroundings.

The origin of double discontinuities near the slab may in part be due to lateral smearing of a step offset in the phase boundary on either side of the slab (i.e., aliasing of structure). Alternatively, H_2O content should be highest at the slab, which may give rise to a localized melt layer atop the 410-km boundary (*16*), with a reflective interface at the top and bottom of the melt layer. The double discontinuity sometimes present near 660-km depth may result from the ringwoodite to Mg-perovskite + magnesiowüstite transition underlain by a weaker discontinuity from the ilmenite (akimotoite) to perovskite transformation, which multi-anvil experiments (*29*) suggest should occur in colder regions. The detection of multiple discontinuities supports the presence of chemical heterogeneity within the mantle and underscores the importance of phase changes in minerals outside the olivine system.

High-resolution mapping of MTZ discontinuities using broadband data reveal a deepened 410-km near subduction, an up-warped 660-km beneath ridges, and multiple reflectors near 410- and 660-km depth. These observations highlight both chemical and thermal heterogeneities in

Earth's upper mantle related to large-scale convective processes.

References and Notes

1. P. M. Shearer, *J. Geophys. Res.* **96**, 18147 (1991).
2. Y. Fei *et al.*, *J. Geophys. Res.* **109**, 10.1029/2003JB002562 (2004).
3. M. Akaogi, E. Ito, A. Navrotsky, *J. Geophys. Res.* **94**, 15671 (1989).
4. E. Ito, E. Takahashi, *J. Geophys. Res.* **94**, 10637 (1989).
5. M. P. Flanagan, P. M. Shearer, *J. Geophys. Res.* **103**, 2673 (1998).
6. J. Gossler, R. Kind, *Earth Planet. Sci. Lett.* **138**, 1 (1996).
7. Y. J. Gu, A. M. Dziewonski, *J. Geophys. Res.* **107**, 2135 (2002).
8. S. Lebedev, S. Chevrot, R. D. van der Hilst, *Science* **296**, 1300 (2002).
9. K. H. Liu, S. S. Gao, P. G. Silver, Y. K. Zhang, *J. Geophys. Res.* **108**, 10.1029/2002JB002208 (2003).
10. J. D. Collier, G. R. Helffrich, *Geophys. J. Int.* **147**, 319 (2001).
11. M. P. Flanagan, P. M. Shearer, *J. Geophys. Res.* **103**, 21165 (1998).
12. N. Schmerr, E. Garnero, *J. Geophys. Res.* **111**, 10.1029/2005JB004197 (2006).
13. Materials and methods are available as supporting material on *Science* online.
14. B. Efron, R. Tibshirani, *Stat. Sci.* **1**, 54 (1986).
15. A. Deuss, S. A. T. Redfern, K. Chambers, J. H. Woodhouse, *Science* **311**, 198 (2006).
16. Y. C. Zheng, T. Lay, M. P. Flanagan, Q. Williams, *Science* **316**, 855 (2007).
17. N. A. Simmons, H. Gurrola, *Nature* **405**, 559 (2000).
18. C. R. Bina, B. J. Wood, *J. Geophys. Res.* **92**, 4853 (1987).
19. L. Stixrude, *J. Geophys. Res.* **102**, 14835 (1997).
20. J. R. Smyth, S. D. Jacobsen, in *Earth's Deep Water Cycle,* S. D. Jacobsen, S. Van der Lee, Eds. (American Geophysical Union, Washington, DC, 2006), vol. 168, pp. 1–11.
21. M. M. Hirschmann, *Annu. Rev. Earth Planet. Sci.* **34**, 629 (2006).
22. S. Karato, in *Water in Nominally Anhydrous Minerals,* H. Keppler, J. R. Smyth, Eds. (Geochemical Society, St. Louis, MO, 2006), vol. 62, pp. 343–375.
23. G. M. Leahy, D. Bercovici, *J. Geophys. Res.* **112**, 10.1029/2006JB004631 (2007).
24. Y. Fei, C. Bertka, in *Mantle Petrology: Field Observations and High Pressure Experimentation,* Y. Fei, C. Bertka, B. Mysen, Eds. (Geochemical Society, Houston, TX, 1999), vol. 6, pp. 189–207.
25. X. Li, S. V. Sobolev, R. Kind, X. Yuan, C. Estabrook, *Earth Planet. Sci. Lett.* **183**, 527 (2000).
26. P. M. Shearer, T. G. Masters, *Nature* **355**, 791 (1992).
27. D. Bercovici, S. Karato, *Nature* **425**, 39 (2003).
28. R. Dasgupta, M. M. Hirschmann, *Nature* **440**, 659 (2006).
29. M. Akaogi, A. Tanaka, E. Ito, *Phys. Earth Planet. Inter.* **132**, 303 (2002).
30. P. Bird, *Geochem. Geophys. Geosys.* **4**, 1027 (2003), 10.1029/2001GC000252.
31. B. Steinberger, *J. Geophys. Res.* **105**, 11127 (2000).

32. We thank A. McNamara and J. Tyburczy for numerous discussions and helpful suggestions, and two anonymous reviewers for their comments. This work was supported by NSF grants EAR-0711401 (E.J.G.) and EAR-0453944 (N.S.) and by an Achievement Rewards for College Scientists Fellowship (N.S.).

Supporting Online Material

www.sciencemag.org/cgi/content/full/318/5850/623/DC1
Materials and Methods
Figs. S1 to S18
References

4 June 2007; accepted 25 September 2007
10.1126/science.1145962

The Impact of Agricultural Soil Erosion on the Global Carbon Cycle

K. Van Oost,[1]*†‡ T. A. Quine,[2]* G. Govers,[1] S. De Gryze,[3] J. Six,[3] J. W. Harden,[4] J. C. Ritchie,[5] G. W. McCarty,[5] G. Heckrath,[6] C. Kosmas,[7] J. V. Giraldez,[8] J. R. Marques da Silva,[9] R. Merckx[10]

Agricultural soil erosion is thought to perturb the global carbon cycle, but estimates of its effect range from a source of 1 petagram per year^{-1} to a sink of the same magnitude. By using caesium-137 and carbon inventory measurements from a large-scale survey, we found consistent evidence for an erosion-induced sink of atmospheric carbon equivalent to approximately 26% of the carbon transported by erosion. Based on this relationship, we estimated a global carbon sink of 0.12 (range 0.06 to 0.27) petagrams of carbon per year^{-1} resulting from erosion in the world's agricultural landscapes. Our analysis directly challenges the view that agricultural erosion represents an important source or sink for atmospheric CO_2.

Humans have drastically altered the global carbon cycle, mostly through increased use of fossil fuels and land use change (*1*). Global earth system models (*2*, *3*) represent well the changes in carbon flux between soil and atmosphere resulting from the reduced carbon inputs to soil and the accelerated decomposition of soil organic carbon (SOC) that accompany conversion of land from an undisturbed state to agricultural use (*4*, *5*). In contrast, the carbon dynamics of the well-documented acceleration of soil erosion and deposition (and resultant lateral fluxes of SOC) associated with conversion of land to agricultural use are poorly understood (*6*).

Soil erosion removes SOC from the site of formation and results in its burial in depositional environments. Recent analyses have identified three key mechanisms whereby these geomorphic processes, together or separately, may result in a change in the net flux of carbon between the soil and atmosphere (fig. S1). Mechanism M1 involves replacement of SOC at eroding sites as a result of continued inputs from plants and decrease in SOC available for decomposition (*6*, *7*); mechanism M2 is the deep burial of allochthonous and autochthonous carbon (*8*) and inhibited decomposition upon burial (*6*, *9*, *10*); and mechanism M3 is the enhanced decomposition of SOC as a result of the chemical or physical breakdown of soil during detachment and transport (*11*). The fundamental controls on the magnitude of the erosion-induced sink or source are then the rate at which SOC is replaced at sites of erosion, changes in the reactivity of SOC as a result of transport and burial, and the rates of soil erosion and deposition. Previous global assessments of the influence of erosion and deposition on carbon dynamics have made markedly different assumptions about these controls, resulting in the diametrically opposed assertions of a global net release or source of 0.37 to 1 Pg C year^{-1} (*12*, *13*) versus a net uptake or sink of 0.56 to 1 Pg C year^{-1} (*6*, *9*, *10*) as a consequence of erosion on agricultural lands.

The controversy about the role of erosion in the global carbon cycle reflects the inherent difficulty of quantifying a net flux controlled by interacting processes that are most often studied in isolation. We examined the integrated effect of the interacting processes using evidence for (i) the rate of SOC replacement at sites of erosion, (ii) the fate of the eroded and buried SOC within agricultural watersheds, and (iii) global soil erosion and soil carbon erosion rates (*14*). The first two lines of evidence were derived from a comprehensive large-scale survey of the SOC and caesium-137 (^{137}Cs) inventories (mass per unit area to given depth) of agricultural soils in Europe and the United States (table S1) that allows us to assess quantitatively the relationships between lateral and vertical SOC fluxes. We examined 1400 soil profiles from 10 watersheds (1 to 14 ha), including noneroded soils and eroding hill slopes as well as colluvial soils where sediment and SOC are buried. The artificial fallout radioisotope

[1]Physical and Regional Geography Research Group, Katholieke Universiteit Leuven, 3001 Heverlee, Belgium. [2]Department of Geography, University of Exeter, EX4 4RJ Exeter, UK. [3]Department of Plant Sciences, University of California, Davis, CA 95616, USA. [4]U.S. Geological Survey, Menlo Park, CA 94025, USA. [5]U.S. Department of Agriculture, Agricultural Research Service, Hydrology and Remote Sensing Laboratory, Beltsville, MD 20705–2350, USA. [6]Department of Agroecology and Environment, Research Centre Foulum, University of Aarhus, 8830 Tjele, Denmark. [7]Laboratory of Soils and Agricultural Chemistry, Agricultural University of Athens, 11855 Athens, Greece. [8]Department of Agronomy, University of Cordoba, 14080 Cordoba, Spain. [9]Instituto de Ciências Agrárias Mediterrânicas, Department of Rural Engineering, University of Évora, Évora, Portugal. [10]Division of Soil and Water Management, Katholieke Universiteit Leuven, 3001 Heverlee, Belgium.

*These authors contributed equally to this work.
†Present address: Département de Géographie, Université Catholique de Louvain, 1048 Louvain-la-Neuve, Belgium.
‡To whom correspondence should be addressed. E-mail: kristof.vanoost@uclouvain.be